



Mechanical response of shear thickening fluid filled composite subjected to different strain rates

Xin Zhang^{a,b}, Pengfei Wang^d, Anatoli Kurkin^e, Qian Chen^d, Xinglong Gong^d, Zhong Zhang^f, En-Hua Yang^{b,*}, Jinglei Yang^{c,*}

^a Department of Mechanics and Aerospace Engineering, Southern University of Science and Technology, Shenzhen, Guangdong 518055, China

^b School of Civil and Environmental Engineering, Nanyang Technological University, 50 Nanyang Avenue, 639798, Singapore

^c Department of Mechanical and Aerospace Engineering, Hong Kong University of Science and Technology, Clear Water Bay, Kowloon, Hong Kong SAR, China

^d CAS Key Laboratory of Mechanical Behavior and Design of Materials, Department of Modern Mechanics, University of Science and Technology of China, Hefei 230026, China

^e School of Materials Science and Engineering, Nanyang Technological University, 50 Nanyang Avenue, 639798, Singapore

^f CAS Key Laboratory of Nanosystem and Hierarchical Fabrication, National Center for Nanoscience and Technology, Beijing 100190, China

ARTICLE INFO

Keywords:

Impact behavior
Energy absorption
Shear thickening fluid
Failure mode

ABSTRACT

Shear thickening fluid (STF) has been used in many areas due to its unique rheological property. In this study, the dynamic mechanical properties of STF-filled composite structures were investigated by in-house fabricated drop weight testing apparatuses. Results indicated that the strength and modulus increase with strain rate for all tube structures. Liquid-filled tubes possess similar strength and modulus, which are larger than air-filled tube at all strain rates. However, STF-filled tube absorbs 5 and 4 times more impact energy than air- and silicone oil-filled tubes, respectively. The energy absorption capacity of STF-filled tube increases with input impact energy. Meanwhile, the shear thickening effect of STF is more sensitive to the loading rate than the input energy, which is an important reference for the designing of STF integrated composite. The STF-filled silicone gel achieves repeatable test due to good protection of the encapsulation, which absorbs 4 times more energy than neat silicone gel during impact. Longitudinal symmetrical profile can be achieved for silicone gel encapsulated STF during impact due to the hardening of the STF which leads to a quick balance state. Moreover, the mechanical response of STF is found to correspond with the rheological performance of the STF.

1. Introduction

Shear thickening fluid (STF) is a non-Newtonian fluid as its shear viscosity increases with shear rate due to hydrodynamics or dilation [1–4]. The STF behaves like a liquid and flows easily at low shear rate. However, dramatic viscosity increase can be observed at higher shear rate which transforms STF from liquid state to solid state [5,6]. Because of the unique property, STF has attracted tremendous research interests [7–9]. STF has shown excellent function in improving turning operation for cutting tool [10], vibration attenuation for composite structures [11,12], polishing operation for steel bar [13], and in protection applications [14,15].

Many researchers impregnate STF into fiber fabrics to enhance energy absorption capacity of the resulting fabrics. Decker et al. [16] studied the drop tower stab resistance of fabrics impregnated with STF against a spike and a knife impactors with an impact velocity of 2 m/s. Results indicated that STF impregnation significantly increased

the puncture resistance of the fabrics against the spike impactor, while slightly improved the stab resistance against the knife impactor. Tan et al. [17] investigated the response of STF impregnated Kevlar fabric under ballistic impact with velocity ranging from 40 to 100 m/s. They found the Kevlar fabrics impregnated with STF can absorb more impact energy than the neat Kevlar fabrics due to their shear thickening properties. Scientists believe that STF may help to restrict the relative motion of the filaments and the yarns, which obstruct the impactor from pushing the yarns out during the penetration [16,18]. Park et al. [14] and Khodadadi et al. [19] investigated the penetration resistance of Kevlar fabric impregnated with STF through numerical simulation, assuming the STF only provided friction between contacted yarns in the fabrics. This assumption provides an easy way to evaluate the fabric impregnated with STF but may cause loss of accuracy in other authentic applications and more discussions on the energy absorption mechanism should be carried out.

Due to the excellent performance of STF-impregnated fiber fabric against low velocity impact, it is of great importance to understand the

* Corresponding authors.

E-mail addresses: ehyang@ntu.edu.sg (E.-H. Yang), maeyang@ust.hk (J. Yang).

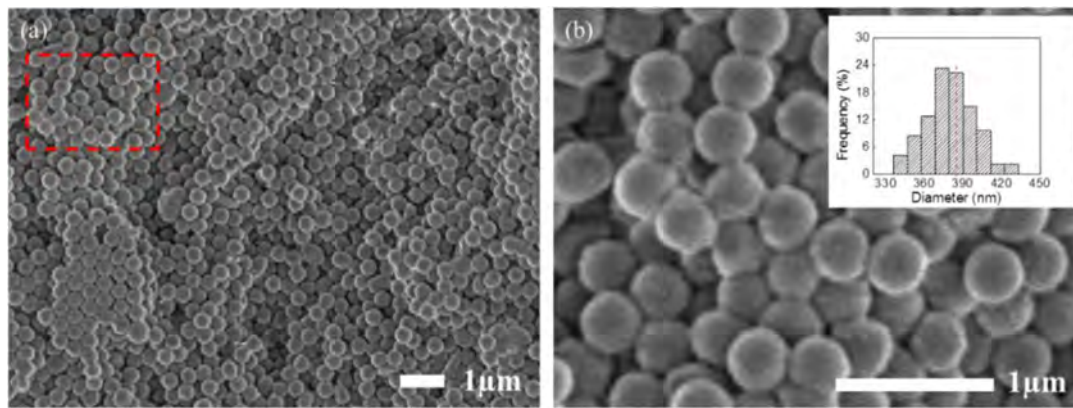


Fig. 1. SEM images and size distribution for fabricated nanoparticles.

mechanical properties of STF under dynamic loading. It is also significant to compare the STF with other Newtonian fluid to further understand the mechanism of shear thickening phenomenon. However, the mechanical properties of the STF without fabric under low velocity impact is not reported sufficiently. Rheological tests have been widely applied to evaluate the shear thickening effect of STF [20]. Few researchers have employed modified split-Hopkinson pressure bar (SHPB) to study the dynamic mechanical properties of STF. Asija et al. [21] and Fu et al. [22] carried out the dynamic test on STF at ultra-high strain rate (8,000 to 21,000 s^{-1}) by using modified SHPB. Results indicated that the toughness of STF increased gradually with the strain rate.

It is of great importance to systematically investigate the mechanical properties of STF under both quasi-static and dynamic loading. Due to the flowability of STF, it is difficult for the STF to remain in a constant regular shape, which is important in evaluation of mechanical property of materials. Meanwhile, due to the moisture absorption nature of STF, better protection of the STF should be applied to investigate the mechanism of shear thickening effect during authentic application (e.g. body armor, smart structure, sports facility, etc.). As a result, in this study, STF was sealed into plastic tube and silicone gel for shape retention, easy handling, protection, and evaluation. Air, deionized (DI) water, and silicone oil were also sealed in the tube for comparison purposes to investigate the influence of the tube structure as well as the hydrostatic pressure condition. Different impact energy was applied to evaluate the mechanical response of STF-filled tubes. High speed camera was employed to investigate the deformation process and fracture mode of STF composite.

2. Materials and method

2.1. Materials

The shear thickening fluid can be fabricated by mixing nanoparticles with a polar solution. To obtain excellent shear thickening property, the nanoparticles were fabricated in the laboratory [23,24]. The chemicals used in the synthesis of STF were purchased from Sinopharm Chemical Reagent Co. Ltd. Firstly, styrene, ethyl acrylate, acrylate, and distilled water were mixed and stirred for 30 min. Then, potassium persulfate was added to the mixture and the reactor was heated to 75°C in a water bath for 6 h. After the centrifugation of the resultants, the polystyrene ethyl acrylate (PSt-EA) particles were rinsed in ultrasonic cleaner and dried in a vacuum oven at 50°C. The resulting PSt-EA particles are spherical (Fig. 1) with a narrow particle size distribution (inset of Fig. 1b) which shows a narrow distribution. The average diameter of the nanoparticles is 385 ± 18 nm. The fabricated nanoparticles are dispersed into anhydrous ethylene glycol (EG) to form the STF. The mixed colloidal suspension with 58.53% of particles by volume was milled and rubbed for 24 h in a ball mill to disperse the PSt-EA particles.

DI water produced from the laboratory and silicone oil from Sigma-Aldrich were used as the reference materials in this study. Polypropylene tube with a diameter of around 4.8 mm and a shell thickness of around 0.12 mm was used as the carrier of core materials. Transparency film from TRI-WIN and epoxy resin from Araldite was used to seal the core materials in the tube. Silicone dielectric gel (Sylgard 527, Dow Corning, Midland, MI, USA) was applied to investigate the mechanical response of STF-filled silicone gel. The silicone gel consisted of a gel base as part A and catalyst as part B with a density of about 0.97 g/cm^3 .

2.2. Specimen preparation

The core materials were filled into the polypropylene tube to the full and sealed with the transparency film by using epoxy resin to form a tube specimen with a diameter of about 4.8 mm and a height of about 4.5 mm, as shown in Fig. 2a3. STF core was also filled into silicone gel to form a gel specimen. Silicone gel was prepared by mixing part A and part B with a weight ratio of 1:1. The mixed silicone gel was heated at 125°C for 75 min in a mold to encapsulate the STF, as instructed by the manufacturer. The diameter of silicone gel composite is around 13 mm and the height is around 7.5 mm.

2.3. Rheological characterization

The rheological properties of DI water, silicone oil, and STF were measured using a rotational rheometer (DHR, TA Instruments, USA) with parallel plates and a 0.3 mm measurement gap with a constant increase of shear rate at room temperature of 25°C, as illustrated in Fig. 2e.

2.4. Mechanical testing

The quasi-static compression tests on the tube and the gel specimens were carried out by an Instron 5569 mechanical tester. A universal head was used to ensure axial loading is applied to the specimen during the compression, as shown in Fig. 2a1 and a2.

The dynamic compression tests on the tube specimens were evaluated by an in-house designed drop weight tester, as shown in Fig. 2b1. The drop weight tester consisted of an aluminum drop bar with a diameter of 12.7 mm, a slide guide, and two polyvinylidene fluoride (PVDF) piezoelectric films (20 mm by 20 mm) connected to an oscilloscope (DLM2000, Yokogawa) for the recording of the impact load. A high speed camera (Fastcam SA4, Photron) with the macro lens was used to capture the deformation and damage evolution of the specimen during impact at a sampling rate of 10^5 frames per second, as illustrated in Fig. 2b2. The aluminum drop bar can be dropped freely in the slide guide and the initial impact velocity can be determined through the images captured by the high speed camera. The velocity of the impactor

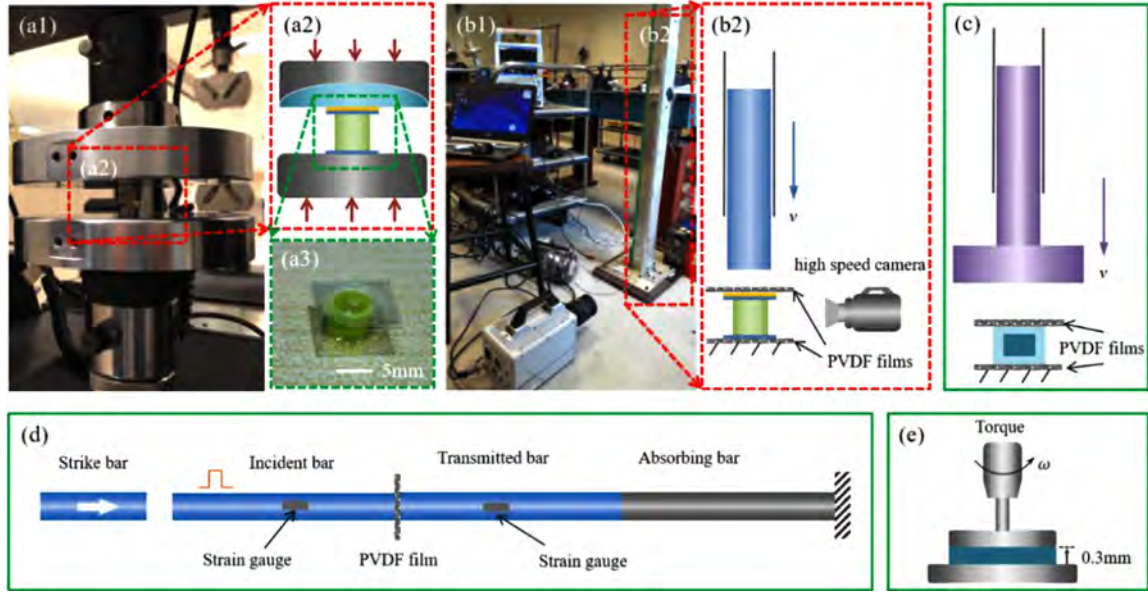


Fig. 2. Testing apparatuses of (a) quasi-static compression test, (b) drop weight test for tube specimen, (c) modified drop weight test for gel composite specimen, (d) SHPB for PVDF films calibration, and (e) rheometer for liquid specimen.

during the impact can be determined by the momentum conservation law as follows,

$$F \cdot t = m \cdot v_t \quad (1)$$

where F is the impact load captured by the PVDF film, t is the recording time, m is the weight of the aluminum impactor, v_t is the corresponding velocity of the impactor. The deformation of the specimen (S) can be calculated through the following equation,

$$S = \int_0^t v_t dt \quad (2)$$

The stress and strain curve of the tube specimen can be derived from the measured load and deformation during the impact.

Due to the high deformability of the gel specimen, an in-house designed “T” shape drop weight tester was used to study the performance of gel specimens under impact, as shown in Fig. 2c. The diameter of the front cylinder of the T shape impactor is 50.8 mm and the weight of the impactor is 148.1g. The gel specimen is sandwiched between two PVDF films (30 mm by 30 mm) to capture the impact load. A similar method as described in the above mentioned drop weight tester (Fig. 2b) is used to determine the stress and strain curve of the gel specimen during impact.

The PVDF films were calibrated by using a split-Hopkinson pressure bar (SHPB) system [25], as illustrated in Fig. 2d. The PVDF films are placed between the incident bar and the transmitted bar without any gap. The strike bar is driven by a high pressure gas gun and generated a stress wave in the incident bar. The generated stress wave propagates to the transmitted bar through the PVDF films. The load was recorded by the PVDF films and compared with that measured by the strain gauges on the incident and the transmitted bars. The stresses in the incident bar (δ_I) and transmitted bar (δ_{II}) can be calculated by the following equations,

$$\delta_I = E \cdot \epsilon_t \quad (3)$$

$$\delta_{II} = E \cdot (\epsilon_i + \epsilon_r) \quad (4)$$

where E is Young's modulus of the bar material, ϵ_t is the strain induced by the transmitted wave, ϵ_i is the strain induced by the incident wave, and ϵ_r is the strain induced by the reflected wave. The contact force recorded by the strain gauge can be calculated as,

$$F_{Gauge} = \delta \cdot A \quad (5)$$

where A is the cross-sectional area of the bar. The contact force measured by the PVDF film can be calculated using the following equation,

$$F_{PVDF} = K \cdot V_t \quad (6)$$

where K is the amplify factor and V_t is the voltage output from the PVDF film. By comparing the load captured by the PVDF films and the strain gauges, the amplify factor K is determined to be 88.1 and 121.3 for the PVDF films in tube and silicone specimen impact, respectively, in the current study. As can be seen from Fig. 3a, the load measured from the incident bar, transmitted bar, and PVDF films fit well with each other, which indicates an equilibrium state during the calibration and good accuracy of the PVDF film.

3. Results and discussion

3.1. Rheological properties

The rheological properties of DI water, silicone oil, and STF were evaluated using the rheometer. As can be seen from Fig. 3b, the viscosities of both the DI water and the silicone oil remain constant regardless of shear rates, suggesting both liquids are Newtonian fluid. It is worth noting that the viscosity of the silicone oil (10.01 Pa·s) is four orders higher than that of the DI water (0.001 Pa·s). At a low shear rate ($< 110 \text{ s}^{-1}$), the viscosity of STF reduces slightly with shear rate due to shear thinning of the liquid medium. When the shear rate exceeds 110 s^{-1} ; however, the viscosity of STF increases dramatically. The corresponding shear rate is also known as the critical shear rate. Meanwhile, the initial viscosity of STF is similar to that of silicone oil.

Electrostatic and Brownian forces between the nanoparticles in the STF may promote the flow of the particles in the liquid medium, which behaves shear thinning effect at a low shear rate [26]. However, the nanoparticles are subjected to hydrodynamic forces at a higher shear rate according to the hydro-clustering theory [27]. The hydrodynamic forces generate the hydro clusters of nanoparticles in the STF suspension, which prevents the free flow of the particles in the liquid medium. Consequently, the viscosity of the suspension may increase dramatically after the critical shear rate [28], as shown in Fig. 3b.

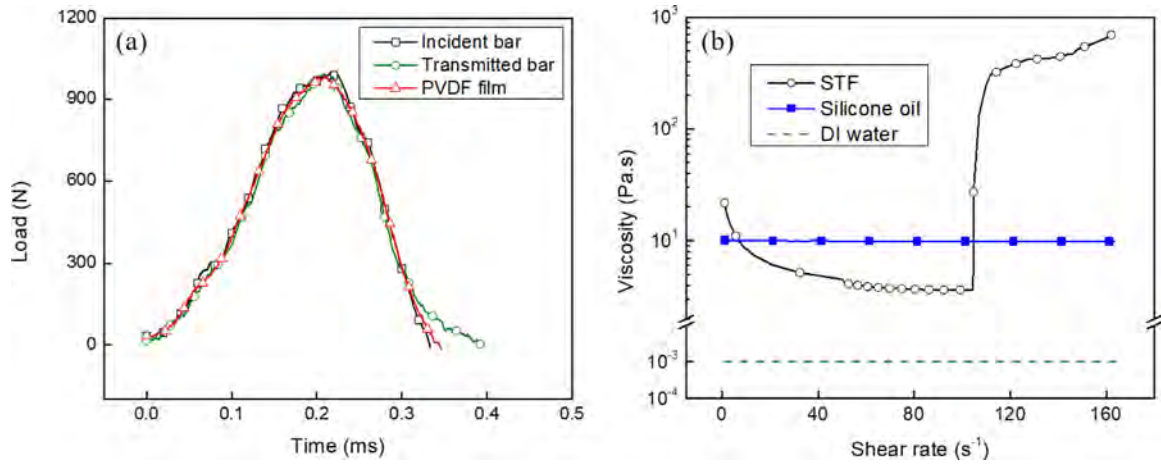


Fig. 3. (a) calibration of PVDF film through SHPB; (b) Viscosity of DI water, silicone oil, and STF at different shear rates.

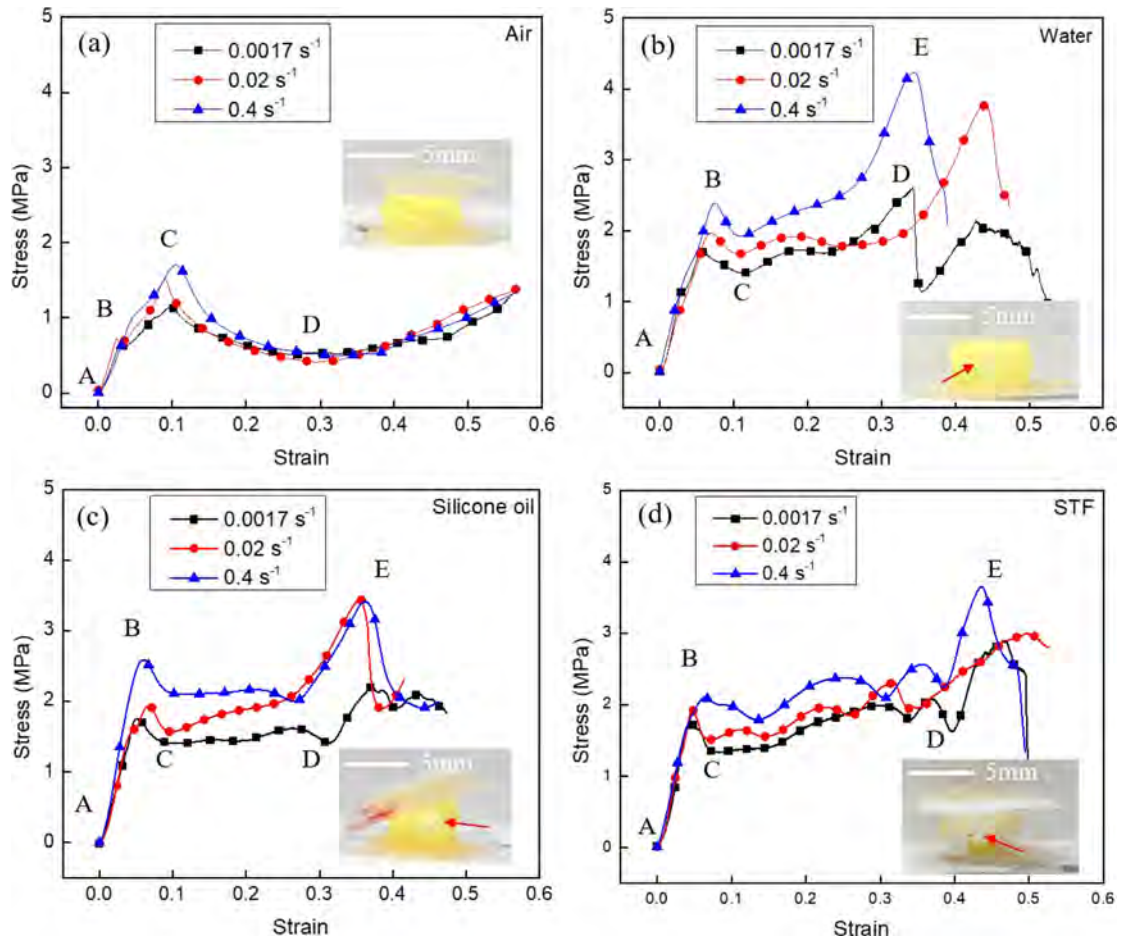


Fig. 4. Typical stress-strain curves of tube specimen at low rate compression.

3.2. Compressive behavior of tube specimen at different strain rates

Typical stress versus strain curves of the tube specimens under low rate compression can be found in Fig. 4. For the air-filled tube (Fig. 4a) at lower strain rates (0.0017 and 0.02 s^{-1}), the stress increases rapidly at the initial stage with a small sudden load drop at point B perhaps due to the formation of a few local buckling because of unbalancing deformation. After which, the stress increases continuously and reaches the peak stress at point C. Under higher strain rates (0.4 s^{-1}), however, the stress increases from point A to point C directly without signs of

sudden load drop. This may be attributed to higher loading rate and there is not sufficient time for the formation of local buckling in the tube specimen. After point C, the stress decreases rapidly due to buckling and lack of support from the tube. At the strain around 0.3 (point D), part of the tube structure may be condensed which leads to increased stress thereafter. After the compression test, severe buckling without obvious cracking and fracture can be found in the air-filled tube (Fig. 4a).

For the liquid-filled tube specimen, the stress increases directly to peak stress (point B) without sudden load drop perhaps due to prevention of local buckling at an early stage. However, slight decrease in the

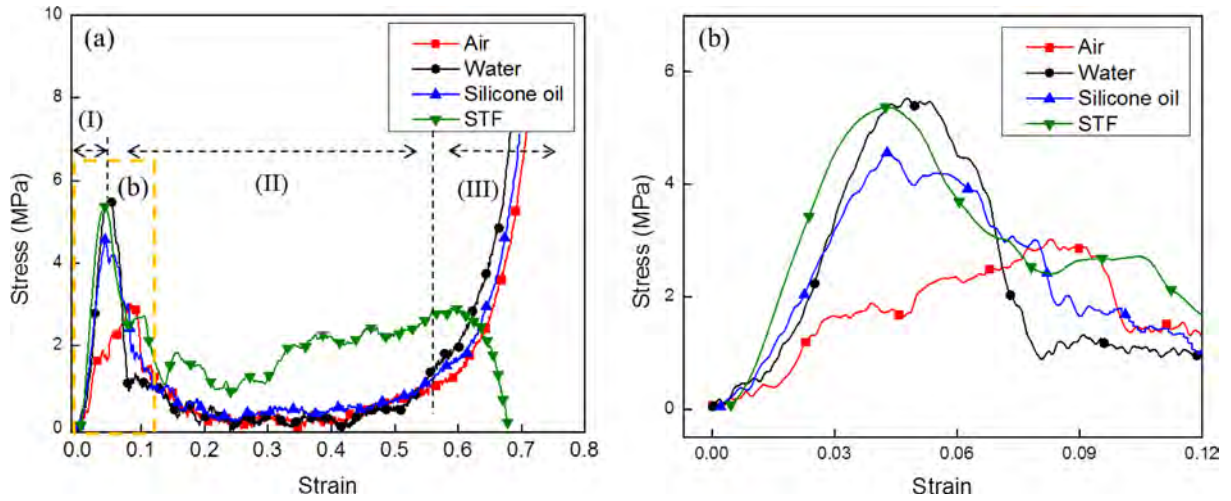


Fig. 5. (a) Typical stress-strain curve of tube composite at impact, (b) enlarged curve at early impact stage.

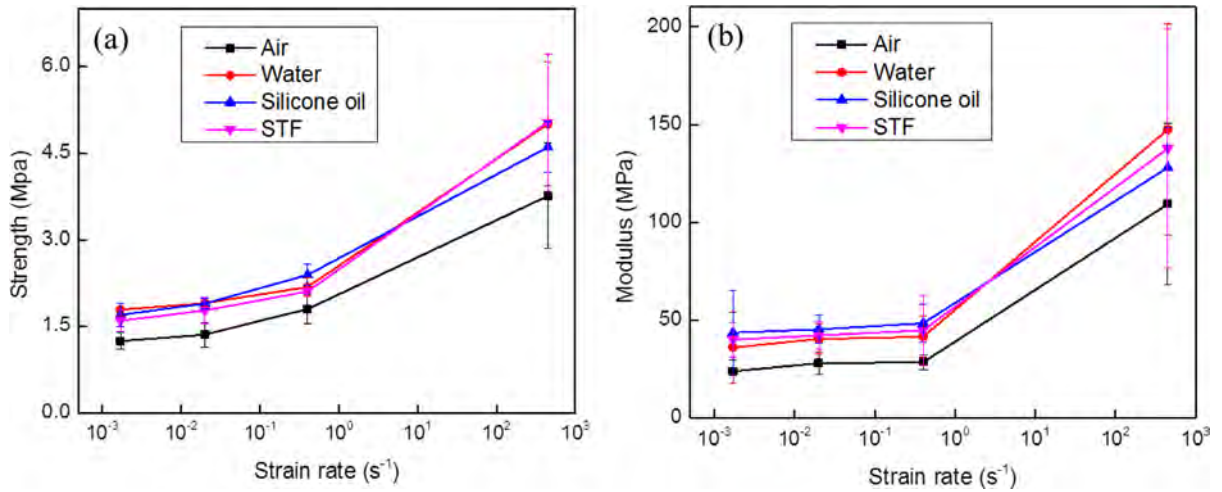


Fig. 6. (a) Strength and (b) modulus of tube composite at different strain rates.

stress (point C) can be observed after the peak stress. Partial buckling of the tube structure or leakage of the liquid is sometimes observed after later stage (i.e., from point C to point D), which leads to a slight drop in the stress during the compression. The stress may increase again until the burst of the tube due to the increased hydrostatic pressure inside the tube (point E), which may cause a sudden drop in the stress. Unlike the air-filled tube specimens, after the compression test, one single crack or fracture point can be observed in the liquid-filled tube specimen, as indicated in red arrows in Fig. 4b–d.

Typical stress versus strain curve of the tube specimens under impact can be found in Fig. 5a. For air-, water-, and silicone oil-filled tube specimens, the compression process can be divided into three stages. The curve in the first (I) stage exhibits a linear increase to an apex, which corresponds to the elastic behavior of the structure [29]. The curve in the second (II) stage reveals a stress drop due to the burst of the tube followed by a plateau due to the stable buckling of the tube structure [30]. The curve in the third (III) stage appears a significant increase in the stress due to the densification of the crushed structure [31]. However, for the STF-filled tube specimen, the compression process can be classified into two stages. The curve in the first (I) stage also shows a linear increase until an apex. After which, in the second (II) stage, the stress drops first and then maintains at a certain level due to the shear thickening effect of the STF. After the second (II) stage, the stress drops again due to the full absorption of the impact energy. The enlarged

stress-strain curves of the tube specimen under impact can be found in Fig. 5b. As can be seen, the stresses of the liquid-filled tube specimens at lower strain (0–0.12) are similar to each other and are higher than that of the air-filled tube specimen. The air-filled tube specimen exhibits a lower stiffness in stage I due to buckling.

The strength of the tube specimen can be calculated by using the following equation,

$$\sigma_s = \frac{F_{peak}}{A_{tube}} \quad (7)$$

where F_{peak} is the peak load in stage I during the impact, A_{tube} is the cross-sectional area of the specimen.

As can be seen in Fig. 6a, the strength of the tube specimen shows strong strain rate sensitivity and increases with strain rates. The liquid-filled tube specimens have comparable strength which is higher than that of the air-filled tube specimen because the core liquid produces hydrostatic pressure to support the tube and increases the stability of the wall by delaying local buckling. The elastic modulus of the tube specimen is defined as the slope of the stress-strain curve at the initial strain part (0–0.03). As can be seen in Fig. 6b, the modulus of the tube specimens also shows strong strain rate sensitivity and increases with strain rate. The liquid-filled tube specimens have a comparable modulus which is higher than that of the air-filled tube specimen for a similar reason.

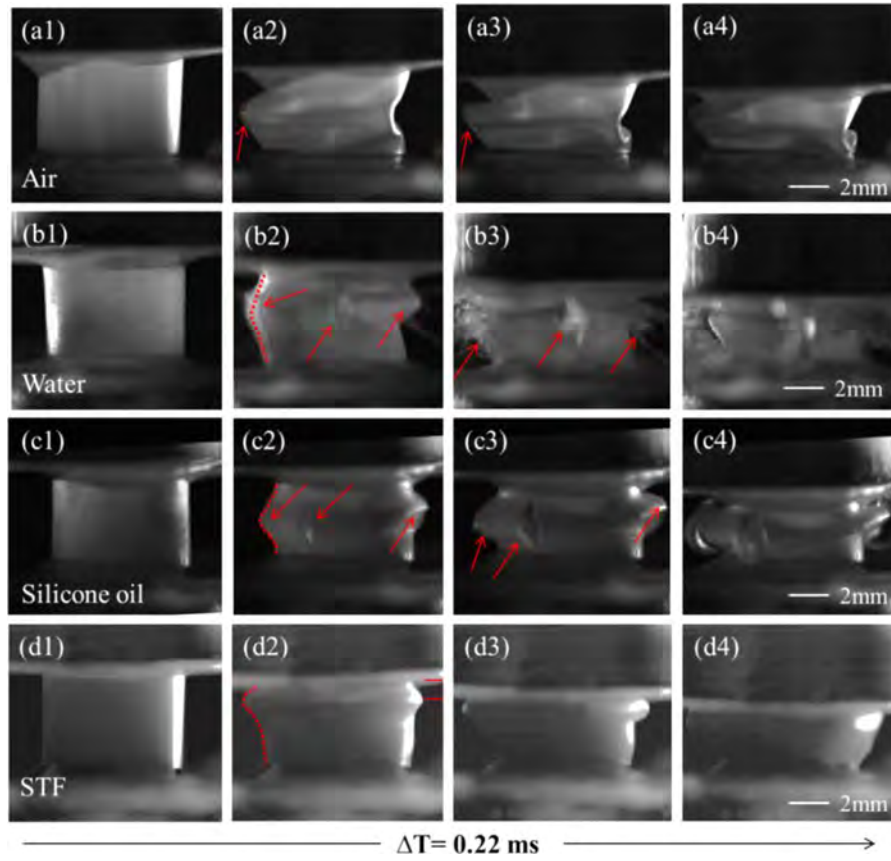


Fig. 7. Deformation and fracture profiles of tube specimen during impact

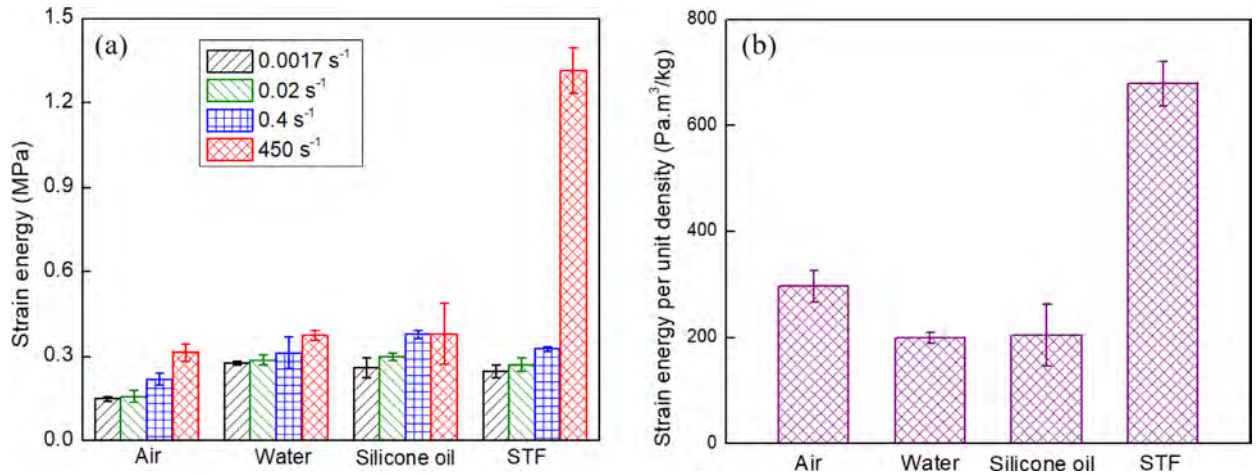


Fig. 8. (a) Strain energy absorption of tube specimens under different loading rates, (b) strain energy absorption per unit density of tube specimens under the impact.

The shear rate during the compression can be estimated by dividing the compression velocity by the thickness of the specimen [32], which is approximately the strain rate during the compression. As a result, the lower strain rates (0.0017 to 0.4 s⁻¹) in the experiments are all below the critical shear rate (110 s⁻¹) of the fabricated STF. As can be found from the rheological test (Fig. 3b), the STF still behaves a liquid state and shows little increase in both strength and modulus. However, during high strain rate loading (450 s⁻¹) which is above the critical shear rate, the shear rate is high enough to trigger the shear thickening phenomenon. The compressed STF may transit from liquid state to solid state and provides the tube structure much higher strength and modulus than the air-filled, water-filled, and silicone oil-filled tubes. Consequently, the STF-filled tube performs superior mechanical proper-

ties under impact than the other tube composites. This finding can also validate the testing methodology adopted for the mechanical characterizations in this study.

3.3. Deformation process and strain energy absorption of tube composite

Fig. 7 shows the deformation process of tube specimens during impact. As can be seen, the air-filled tube specimen deformed unsteadily at the early strike stage, as shown in Fig. 7a2. One single crack along the impact direction was observed as indicated in the red arrow, which is different from the failure model under low rate compression (i.e., severe buckling without cracking as shown in Fig. 4a). The tube buckled

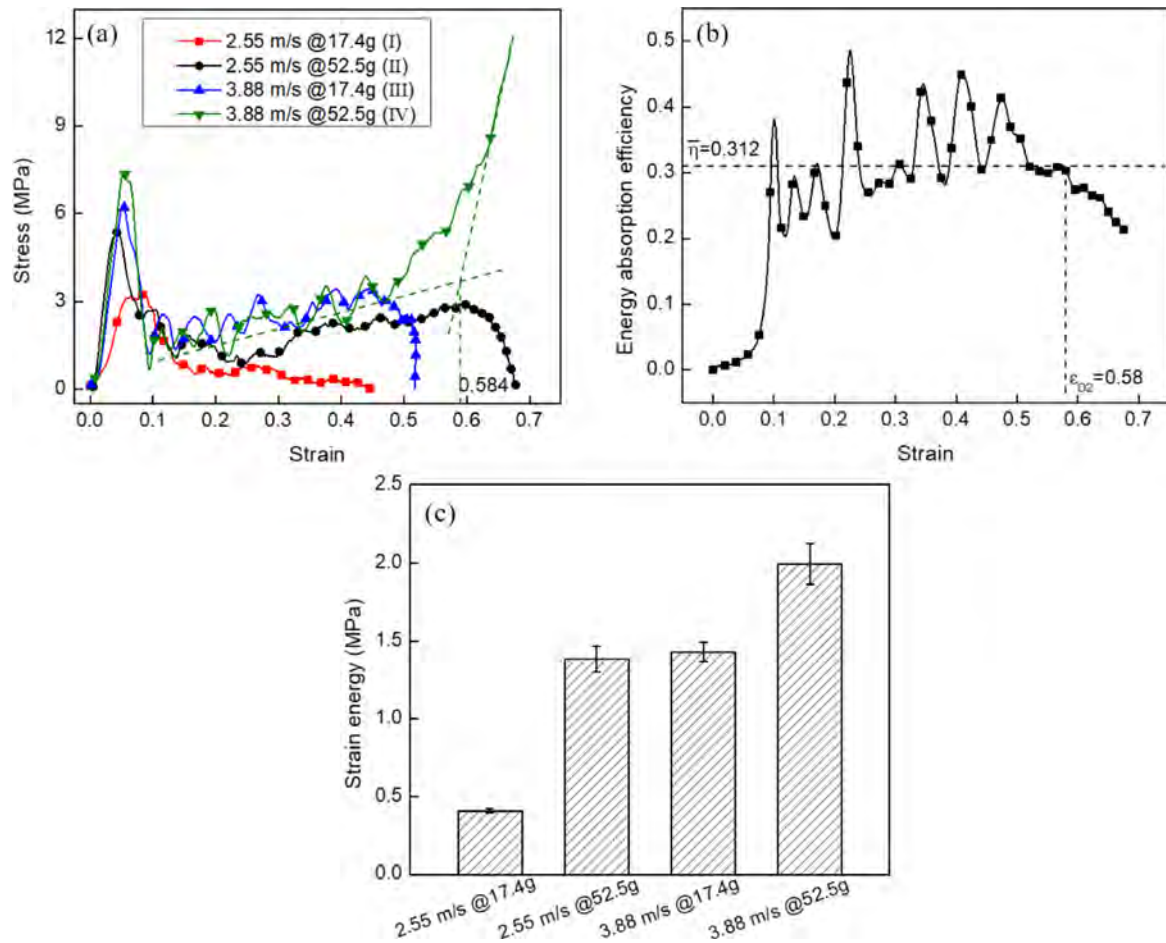


Fig. 9. (a) Typical stress versus strain of tube composite at different loading conditions; (b) energy absorption efficiency of test at condition IV; (c) strain energy absorption at different loading conditions.

continuously which led to low stress level in the second (II) stage as indicated in Fig. 5a.

Different failure mode was observed in the water-filled tube specimen as more cracks distributed equally on the tube surface (as indicated by red arrows) were observed, which suggests the tube experienced a more uniform loading during impact than that during low rate compression (Fig. 4b). The fractured tube tended to protrude outward during the impact. A relatively symmetric deformation profile could be observed as indicated by the red dash line in Fig. 7b2. The water ejected out the tube quickly from the cracks. After the fracture of the tube structure, the stress decreases to a low level in the second (II) stage similar to that of the air-filled tube specimen as indicated in Fig. 5a, which shows that the water may not provide support after the fracture of the tube.

The deformation of the silicone oil-filled tube specimen can be found in Fig. 7c, which is similar to that of the water-filled tube specimen. Evenly distributed cracks (as indicated by red arrows) occurred at the impact direction and a symmetric deformed profile could be observed as can be seen in Fig. 7c2. However, due to the higher viscosity of the silicone oil, the oil comes out of the tube at a slower speed during the impact. Similarly to the water-filled tube specimen, after the fracture of the tube structure, the stress decreases to a low level in the second (II) stage similar to that of the air-filled tube specimen as indicated in Fig. 5a, which suggests that the use of liquid with higher viscosity, such as silicone oil, alone still cannot stand much force during the impact.

Distinctive deformation process and failure mode can be observed in the STF-filled tube specimen as depicted in Fig. 7d. An unsymmetrical deformation profile can be observed as the impact front of the tube is larger than the bottom side at the early stage (Fig. 7d2). Part of the STF

is squeezed out from the tube due to fracture of the tube at the top cover (Fig. 7d3). The STF behaves like solid material during the entire impact process which leads to higher stress level in the second (II) stage during the impact, as shown in Fig. 5a. No obvious cracks can be observed in the STF-filled tube specimen due to shear thickening effect. The squeezed STF remains solid state during the impact to absorb the impact energy.

The strain energy at different strain rates is obtained by calculating the area under the stress-strain curve up to a strain of 0.4 (i.e., before the densification of the tube specimen) [23] as shown in Fig. 8a. The liquid-filled tube specimens constantly show higher energy absorption capacity than the air-filled tube specimen at all strain rates. This is because the core liquid can provide hydrostatic pressure during the impact which can absorb more impact energy. For the air-filled tube specimen, the strain energy increases with strain rate due to the strain rate effect of the polypropylene tube material [33,34] and the enclosed gas [35,36]. Similarly, the strain energy of the water-filled and the silicone oil-filled tube specimens also increases with strain rates. The strain energy of the water-filled tube specimen is similar to that of the silicone oil-filled tube specimen, which implies that the viscosity of the liquid core does not have a strong influence on the energy absorption capacity of the tube specimen. For the STF-filled tube specimen, the strain energy capacity increases slightly with the strain rate at low rate compression. However, a significant increase was observed at impact, which reveals that the thickening effect of the STF under dynamic loading remarkably enhances the energy absorption capacity of the tube specimen.

That is because when the STF is subjected to quasi-static loading, the shear rate is below the critical shear rate and the liquid phase is still dominated which makes the energy absorption similar to the water-

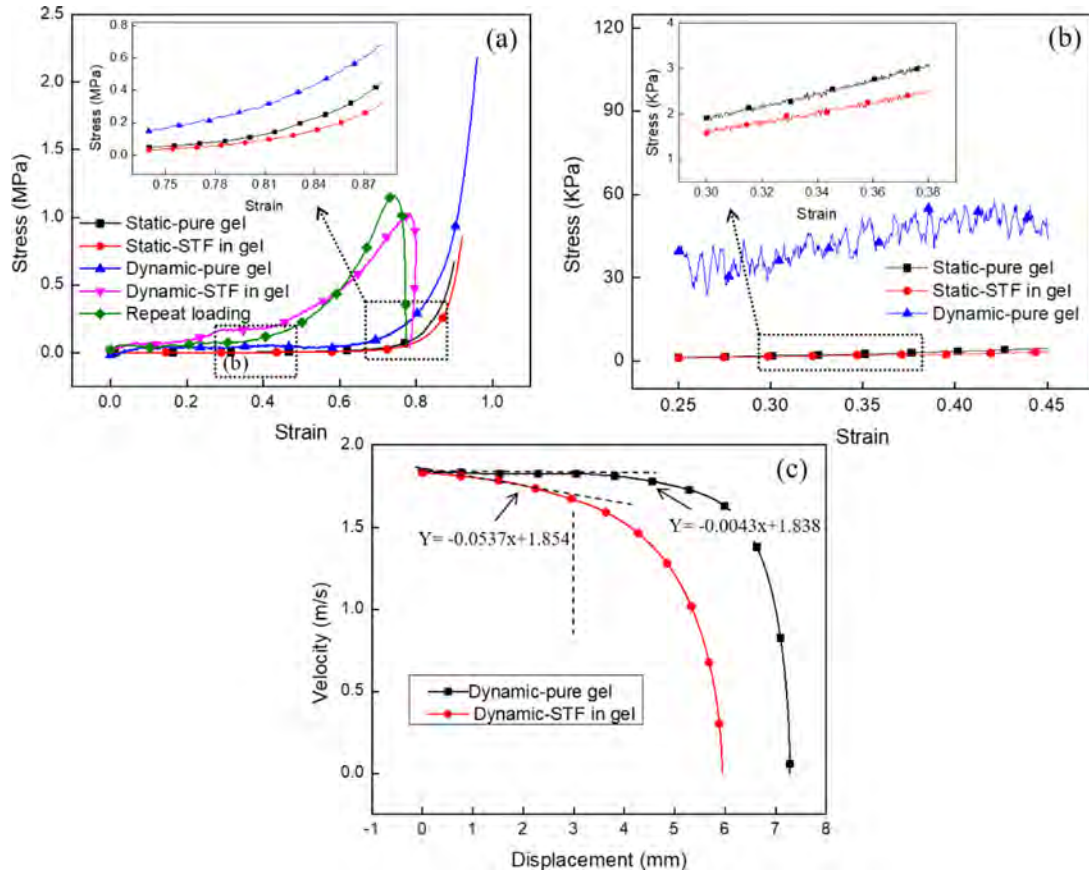


Fig. 10. (a) Typical stress-strain curves of pure gel and STF filled gel at both quasi-static and dynamic loading conditions, (b) enlarged image of stress-strain curves, and (c) velocity variation of the impactor.

filled and silicone oil-filled tube. However, during dynamic compression, the subjected shear rate is above the critical shear rate which contributes to a significant energy absorption increase.

The mass effect is also studied by dividing the absorbed strain energy with the density of different tube structures. The density of the tube structure is defined as the overall weight of the tube composite divided by the volume of the cylindrical specimen. After calculation, the densities of air-filled, water-filled, silicone oil-filled, and STF-filled tubes are 1.056×10^3 , 1.876×10^3 , 1.852×10^3 , and $1.937 \times 10^3 \text{ kg/m}^3$, respectively. The strain energy absorption per unit density of different tube specimens under impact loading is shown in Fig. 8b. The water-filled and silicone oil-filled tubes show similar strain energy per unit density, which is smaller than the air-filled tube, due to the mass increase after filling the liquid into the tube structure. However, the STF-filled tube can absorb 129% more strain energy per unit density than the air-filled tube, and 241% more than that of the water-filled tube. The finding confirms the excellent energy absorption capacity of STF-filled tube composite under the impact compared with Newtonian liquid filled-tube and air-filled tube, although it increases the density of the structure.

3.4. Influence of impact energy on the mechanical property of STF-filled tube specimen

Mechanical properties of STF-filled tube specimens under impact are further investigated. Two different impactors with the weight of 17.4g and 52.5g and two different impact velocities at 2.25 m/s and 3.88 m/s were applied to the tube specimens. The loading conditions are summarized in Table 1. As can be seen, conditions II and III have comparable input energy while conditions III and IV have identical impact velocity (and thus similar loading rates).

Table 1
Loading conditions for impact tests.

Condition	Velocity (m/s)	Weight (g)	Input energy (KJ)
I	2.25	17.4	44.0
II	2.25	52.5	132.9
III	3.88	17.4	131.0
IV	3.88	52.5	395.2

Typical stress-strain curves at different loading conditions can be found in Fig. 9. Under loading condition I with the least impact energy and loading rate, peak stress was observed followed by continuous stress reduction due to the consumption of the input energy by the tube structure and thickening effect of the STF. Under loading conditions II and III, plateau stress was observed after the peak stress due to the stronger thickening effect of the STF, which allows absorption of more impact energy. Compared to loading condition II, higher post-peak stress was observed under loading condition III, which is comparable to that under loading condition IV. This suggests that the thickening of STF is more related to the loading rate than the input energy, which indicates that the loading rate is the dominant factor in the input energy in influencing the mechanical properties of STF structures. Under loading condition IV with the highest impact energy and loading rate, the stress increases rapidly after the plateau stress due to the densification of the tube structure. The densification strain ($\epsilon_D=0.584$) [23,37] can be determined by taking the intersection of tangents to the stress-strain curve as shown in Fig. 9a. To verify the densification strain, energy absorption efficiency factor (η_e) [38] is checked as shown in Fig. 9b, which is defined as fol-

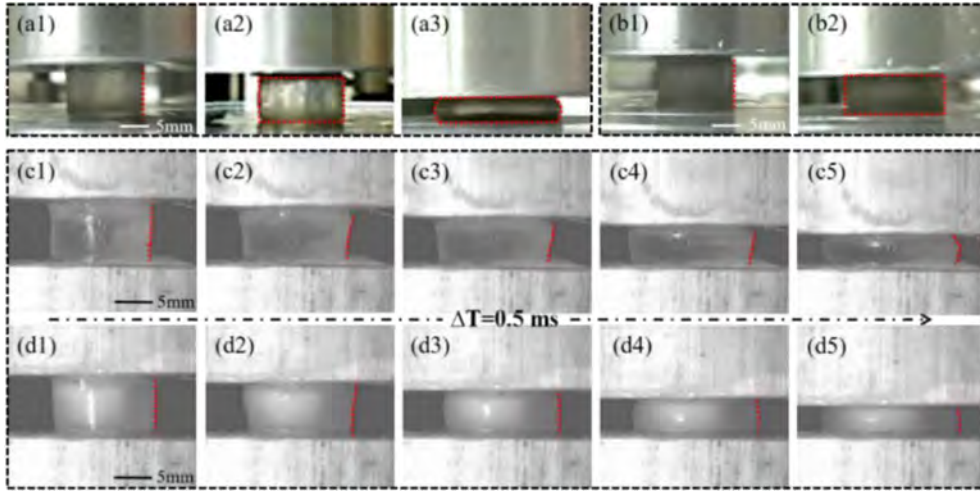


Fig. 11. Deformation profiles of pure silicone gel and encapsulated STF at quasi-static compression and impact loading.

lows,

$$\eta_\epsilon = \frac{1}{\sigma_\epsilon} \int_0^\epsilon \sigma_\epsilon d\epsilon \quad (8)$$

where σ_ϵ is the stress at specific strain ϵ .

As can be seen from Fig. 9b, the value of η_ϵ increases rapidly at the initial impact stage and remains at a high level till the strain around 0.58, which is close to the value obtained from the intersection method. For specimen under the loading condition IV, the energy absorption is calculated by integrating the stress-strain curve up to the densification strain. For specimens under other loading conditions, the energy absorption is calculated by calculating the entire area under the stress-strain curve. The resulting strain energy of the STF-filled tube specimen under different loading conditions can be found in Fig. 9c. As can be seen, the input energy can be completely absorbed by the tube specimen under the loading conditions I to III. Even higher strain energy is observed under the loading condition IV, which indicates that more energy can be absorbed by the STF at higher impact energy. However, due to the densification of the tube structure, the absorbed energy in condition IV can be regarded as the maximum energy that can be absorbed by the STF-filled tube composite.

The STF-filled tube specimen can absorb 5.33 times energy than the air-filled tube specimen and 4.04 times energy than the silicone oil-filled tube under the impact. However, the STF-filled tube specimen was damaged after only one impact, which led to the leakage of the core STF material. It is of great interest to develop an STF-filled material that can provide better isolation of the core STF and sustain multiple impacts. As a result, the STF was encapsulated into silicone gel for further evaluation.

3.5. Mechanical behaviors of STF-filled silicone gel

Typical stress-strain curves of STF-filled silicone gel and pure silicone gel subject to quasi-static and impact loads are plotted in Fig. 10. As can be seen, the curve of pure silicone gel under quasi-static load, the curve of pure silicone gel under the impact, and the curve of STF-filled silicone gel under quasi-static load are similar. The stress is relatively small before the strain of 0.7. The enlarged image (Fig. 10b) reveals that the stress of pure silicone gel specimen under impact is slightly higher than that under quasi-static load, suggesting strain rate sensitivity of silicone gel. Furthermore, under quasi-static loading, the stress of pure silicone gel specimen is slightly higher than that of STF-filled silicone gel specimen perhaps due to the liquid state of STF subject to low rate compression. The stress-strain curve of the STF-filled silicone gel specimen can be found in Fig. 10a. The thickening of the STF may dramatically increase the stress in the STF-filled silicone gel, as indicated

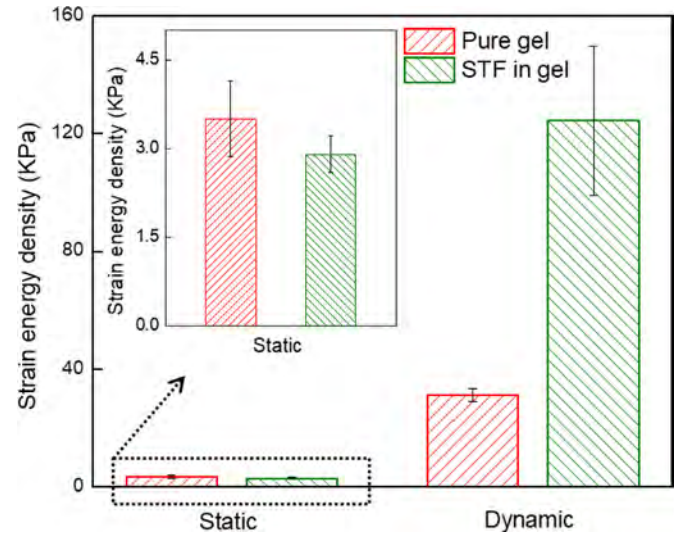


Fig. 12. Strain energy density of pure silicone gel and STF-filled silicone gel specimens at quasi-static and dynamic loadings.

by the pink line. The change of impactor velocity during impact can be found in Fig. 10c. As can be seen, at the displacement of less than 3 mm, the decreasing rate of impactor velocity for the STF-filled silicone gel is one order higher than that for the pure silicone gel. It reveals that the STF can significantly increase the impact resistance of the STF-filled silicone gel specimen. The encapsulated STF can also be reused after the 1st impact as there is no obvious fracture, which implies that the silicone gel encapsulates the core material well during the impact. The repeated stress-strain curve of the STF-filled silicone gel specimen can be found in Fig. 10a. As can be seen, the stress-strain curve of the repeated impact loading fits well with the curve of the specimen during the first impact. The STF-filled silicone gel remains unfractured even after five times' impact. The repeatable compressive property is very important in the protection and the authentic application of the STF.

The deformation profile at quasi-static loading can be found in Fig. 11a and b. Symmetrical profiles can be observed for both the pure silicone gel and the STF-filled silicone gel, which indicates a balance deformation during the compression process. The different profiles can be found for the pure silicone gel at impact loading as shown in Fig. 11c with a time interval of 0.5 ms. A larger top surface of the silicone gel can be observed till 2 ms after the impact, as can be seen in Fig. 11c2–c4. The deformation profile of the STF-filled silicone gel specimen is also

different as a symmetrical profile can be found as shown in Fig. 11d3–d5. This may be attributed to the thickening of the STF which leads to a more balance deformation under dynamic loading.

The energy absorption capacity of the pure silicone gel and the STF-filled silicone gel specimens under quasi-static as well as impact loads is investigated by calculating the area under the stress-strain curve up to a strain of 0.7. As shown in Fig. 12, only a small amount of energy can be absorbed by the pure silicone gel and STF-filled silicone gel specimen at quasi-static loading. Furthermore, the pure silicone gel has slightly higher energy absorption capacity than the STF-filled silicone gel due to the STF is in its liquid state during quasi-static compression. More energy can be absorbed by the pure silicone gel under impact because of the strain rate effect of the silicone gel. Four times more energy can be absorbed by the STF-filled silicone gel than that by the pure silicone gel under impact due to the thickening of STF.

4. Conclusions

In this study, the mechanical performance of STF filled composite was systematically investigated and compared with other non-STF filled composites under different strain rates from quasi-static loading to dynamic loading. An in-house fabricated drop weight testing apparatus was developed to investigate the dynamic mechanical properties of STF specimens. The STF was integrated into structural members to modify the mechanical properties of the members and isolate the STF with the environment to solve the moisture absorption and flowability issue of STF during authentic applications. Results indicated that the strength and modulus increase with strain rate for all tube structures. During the quasi-static compression, the DI water-filled, silicone oil-filled, and STF-filled tube composites show similar trends and values in energy absorption at different strain rates because of the liquid state of STF under quasi-static loading. However, due to the excellent shear thickening effect of the STF at high strain rate, the STF-filled tube structure can absorb much more impact energy than the air-, water-, and silicone oil-filled tube structures. The phenomenon is also related to the rheological property of the fabricated STF. Multiple cracks are distributed evenly along the surface of the liquid-filled tube structure while a single crack is generated in the air-filled tube due to the hydrostatic pressure derived from the liquid core can provide a uniform deformation during the loading. Broad front side in the STF-filled tube can be observed. The energy absorption capacity of the STF-filled tube increases with input impact energy. Meanwhile, the shear thickening effect of STF is more related to the loading rate than the input energy. The STF-filled silicone gel shows a significant strengthening effect during the impact process. Repeatable tests can be carried out because of good protection of the encapsulation process. The STF-filled silicone gel can absorb four times the impact energy than the neat silicone gel. Different deformation modes can be observed due to the solid state transformation of STF during impact.

Declaration of Competing Interest

The authors declare that they have no known competing financial interests or personal relationships that could have appeared to influence the work reported in this paper.

CRediT authorship contribution statement

Xin Zhang: Writing - original draft, Methodology, Conceptualization. **Pengfei Wang:** Validation. **Anatoli Kurkin:** Validation. **Qian Chen:** Data curation. **Xinglong Gong:** Validation, Investigation. **Zhong Zhang:** Validation, Investigation. **En-Hua Yang:** Methodology, Writing - review & editing, Supervision. **Jinglei Yang:** Validation, Writing - review & editing, Supervision.

Acknowledgment

The authors acknowledged the supports from The Hong Kong University of Science and Technology (Grant #: R9365), the NSFC/HK-RGC Joint Research Scheme (Grants #: N_HKUST 631/18 and 51861165103), and Nanhai-HKUST Program (Grant #: FSNH-18FYTR101). Sincere thanks are given to Dr. Youjin Zhou and Dr. Xin Li for their constructive suggestions and supports on this work.

References

- [1] Brown E, Forman NA, Orellana CS, Zhang H, Maynor BW, Betts DE, DeSimone JM, Jaeger HM. Generality of shear thickening in dense suspensions. *Nat Mater* 2010;9:220.
- [2] Cheng X, McCoy JH, Israelachvili JN, Cohen I. Imaging the microscopic structure of shear thinning and thickening colloidal suspensions. *Science* 2011;333:1276–9.
- [3] James NM, Han E, de la Cruz RAL, Jureller J, Jaeger HM. Interparticle hydrogen bonding can elicit shear jamming in dense suspensions. *Nat Mater* 2018;17:965.
- [4] Wei H, Gao H, Wang X. Development of novel guar gum hydrogel based media for abrasive flow machining: shear-thickening behavior and finishing performance. *Int J Mech Sci* 2019;157:758–72.
- [5] Sen S, Shaw A, Deb A. Numerical investigation of ballistic performance of shear thickening fluid (STF)-Kevlar composite. *Int J Mech Sci* 2019;164:105174.
- [6] Majumdar A, Laha A, Bhattacharjee D, Biswas I. Tuning the structure of 3D woven aramid fabrics reinforced with shear thickening fluid for developing soft body armour. *Compos Struct* 2017;178:415–25.
- [7] Sehgal P, Ramaswamy M, Cohen I, Kirby BJ. Using acoustic perturbations to dynamically tune shear thickening in colloidal suspensions. *Phys Rev Lett* 2019;123:128001.
- [8] Wu X, Xiao K, Yin Q, Zhong F, Huang C. Experimental study on dynamic compressive behaviour of sandwich panel with shear thickening fluid filled pyramidal lattice truss core. *Int J Mech Sci* 2018;138:467–75.
- [9] Grgeen S, Li W, Kuşhan MC. The rheology of shear thickening fluids with various ceramic particle additives. *Mater Des* 2016;104:312–19.
- [10] Grgeen S, Sofuoğlu MA. Integration of shear thickening fluid into cutting tools for improved turning operations. *J Manuf Process* 2020;56:1146–54.
- [11] Grgeen S, Sofuoğlu MA. Vibration attenuation of sandwich structures filled with shear thickening fluids. *Compos Part B-Eng* 2020;186:107831.
- [12] Grgeen S, Sofuoğlu MA. Experimental investigation on vibration characteristics of shear thickening fluid filled CFRP tubes. *Compos Struct* 2019;226:111236.
- [13] Grgeen S, Sert A. Polishing operation of a steel bar in a shear thickening fluid medium. *Compos Part B-Eng* 2019;175:107127.
- [14] Park Y, Kim Y, Baluch AH, Kim C-G. Numerical simulation and empirical comparison of the high velocity impact of STF impregnated Kevlar fabric using friction effects. *Compos Struct* 2015;125:520–9.
- [15] Wei M, Sun L, Zhu J. Effects of parameters controlling the impact resistance behavior of the GFRP fabric impregnated with a shear thickening fluid. *Mater Des* 2020;196:109078.
- [16] Decker M, Halbach C, Nam C, Wagner N, Wetzel E. Stab resistance of shear thickening fluid (STF)-treated fabrics. *Compos Sci Technol* 2007;67:565–78.
- [17] Tan Z, Li W, Huang W. The effect of graphene on the yarn pull-out force and ballistic performance of Kevlar fabrics impregnated with shear thickening fluids. *Smart Mater Struct* 2018;27:075048.
- [18] Lee YS, Wetzel ED, Wagner NJ. The ballistic impact characteristics of Kevlar® woven fabrics impregnated with a colloidal shear thickening fluid. *J Mater Sci* 2003;38:2825–33.
- [19] Khodadadi A, Liaghat G, Sabet A, Hadavinia H, Aboutorabi A, Razmkhah O, Akbari M, Tahmasebi M. Experimental and numerical analysis of penetration into Kevlar fabric impregnated with shear thickening fluid. *J Thermoplast Compos Mater* 2018;31:392–407.
- [20] Fu K, Cui X, Zhang Y, Ye L, Chang L, Friedrich K. Confined compression behaviour of a shear thickening fluid with concentrated submicron particles. *Compos Commun* 2018;10:186–9.
- [21] Asija N, Chouhan H, Gebremeskel SA, Bhatnagar N. High strain rate characterization of shear thickening fluids using Split Hopkinson Pressure Bar technique. *Int J Impact Eng* 2017;110:365–70.
- [22] Fu K, Wang H, Wang S, Chang L, Shen L, Ye L. Compressive behaviour of shear-thickening fluid with concentrated polymers at high strain rates. *Mater Des* 2018;140:295–306.
- [23] Zhang X, Zhang H, Wang P, Chen Q, Li X, Zhou Y, Gong X, Zhang Z, Yang E-H, Yang J. Optimization of shear thickening fluid encapsulation technique and dynamic response of encapsulated capsules and polymeric composite. *Compos Sci Technol* 2019;170:165–73.
- [24] Zhang H, Zhang X, Chen Q, Li X, Wang P, Yang E-H, Duan F, Gong X, Zhang Z, Yang J. Encapsulation of shear thickening fluid as an easy-to-apply impact-resistant material. *J Mater Chem A* 2017;5:22472–9.
- [25] Xu Y, Dai F, Du H. Experimental and numerical studies on compression-shear behaviors of brittle rocks subjected to combined static-dynamic loading. *Int J Mech Sci* 2020;175:105520.
- [26] Grgeen S. Tuning the rheology of nano-sized silica suspensions with silicon nitride particles. *J Nano Res* 2019;56:63–70.
- [27] Grgeen S, de Sousa RJA. Rheological and deformation behavior of natural smart suspensions exhibiting shear thickening properties. *Arch Civ Mech Eng* 2020;20:110.

- [28] Gorgen S, Sofuoğlu MA, Kushan MC. Rheological compatibility of multi-phase shear thickening fluid with a phenomenological model. *Smart Mater Struct* 2019;28:035027.
- [29] Xiang X, Lu G, You Z. Energy absorption of origami inspired structures and materials. *Thin-Walled Struct* 2020;157:107130.
- [30] Zhang X, Wang P, Zhou Y, Li X, Yang E-H, Yu T, Yang J. The effect of strain rate and filler volume fraction on the mechanical properties of hollow glass microsphere modified polymer. *Compos Part B* 2016;101:53–63.
- [31] Zhang X, Wang P, Sun D, Li X, An J, Yu T, Yang E-H, Yang J. Dynamic plastic deformation and failure mechanisms of individual microcapsule and its polymeric composites. *J Mech Phys Solids* 2020;139:103933.
- [32] Lu ZQ, Wu LW, Gu BH, Sun BZ. Numerical simulation of the impact behaviors of shear thickening fluid impregnated warp-knitted spacer fabric. *Compos Part B* 2015;69:191–200.
- [33] Alcock B, Cabrera N, Barkoula N-M, Reynolds C, Govaert L, Peijs T. The effect of temperature and strain rate on the mechanical properties of highly oriented polypropylene tapes and all-polypropylene composites. *Compos Sci Technol* 2007;67:2061–70.
- [34] Zhang Z, Hou S, Mao Y, He L, Han X. Rate-related study on the ply orientation of carbon fiber reinforced epoxy composite laminates. *Int J Mech Sci* 2020;188:105968.
- [35] Islam M, Brown A, Hazell P, Kader M, Escobedo J, Saadatfar M, Xu S, Ruan D, Turner M. Mechanical response and dynamic deformation mechanisms of closed-cell aluminium alloy foams under dynamic loading. *Int J Impact Eng* 2018;114:111–22.
- [36] Zhang X, Wang P, Sun D, Li X, Yu T, Yang E-H, Yang J. Rate dependent behaviors of nickel-based microcapsules. *Appl Phys Lett* 2018;112:221905.
- [37] Paul A, Ramamurty U. Strain rate sensitivity of a closed-cell aluminum foam. *Mater Sci Eng* 2000;281:1–7.
- [38] Smorygo O, Marukovich A, Mikutski V, Gokhale A, Reddy GJ, Kumar JV. High-porosity titanium foams by powder coated space holder compaction method. *Mater Lett* 2012;83:17–19.